



HAL
open science

Time Integration and Assessment of a Model for Shape Memory Alloys Considering Multiaxial Nonproportional Loading Cases

Xiaojun Gu, Wael Zaki, Claire Morin, Ziad Mourni, Weihong Zhang

► **To cite this version:**

Xiaojun Gu, Wael Zaki, Claire Morin, Ziad Mourni, Weihong Zhang. Time Integration and Assessment of a Model for Shape Memory Alloys Considering Multiaxial Nonproportional Loading Cases. International Journal of Solids and Structures, 2015, 54, pp.82-99. 10.1016/j.ijsolstr.2014.11.005 . hal-01137441

HAL Id: hal-01137441

<https://hal.science/hal-01137441>

Submitted on 3 Apr 2015

HAL is a multi-disciplinary open access archive for the deposit and dissemination of scientific research documents, whether they are published or not. The documents may come from teaching and research institutions in France or abroad, or from public or private research centers.

L'archive ouverte pluridisciplinaire **HAL**, est destinée au dépôt et à la diffusion de documents scientifiques de niveau recherche, publiés ou non, émanant des établissements d'enseignement et de recherche français ou étrangers, des laboratoires publics ou privés.

Time Integration and Assessment of a Model for Shape Memory Alloys Considering Multiaxial Nonproportional Loading Cases

Xiaojun Gu^a, Wael Zaki^{b,*}, Claire Morin^c, Ziad Moumni^{d,a}, Weihong Zhang^{a,*}

^a*Northwestern Polytechnical University*

127 Youyi West Rd, Xi'an, Shaanxi 710072, China

^b*Khalifa University of Science, Technology, and Research*

P.O. Box 127788, Abu Dhabi, UAE

^c*École Nationale Supérieure des Mines de Saint-Étienne*

158, cours Fauriel

42023 Saint-Étienne, France

^d*ENSTA-ParisTech*

91762 Palaiseau Cedex, France

Abstract

The paper presents a numerical implementation of the ZM model for shape memory alloys (Zaki and Moumni, 2007a) that fully accounts for nonproportional loading and its influence on martensite reorientation and phase transformation. Detailed derivation of the time-discrete implicit integration algorithm is provided, including an explicit closed-form expression for the continuous material jacobian. The algorithm is used for finite element simulations using Abaqus, in which the model is implemented by means of a user material subroutine. Extensive validation of the model is provided against multiple sets of experimental and numerical simulation data taken from the literature.

*Corresponding author. Tel.: +971 2 5018511.

Email addresses: gu.xiaojun@live.cn (Xiaojun Gu), wael.zaki@kustar.ac.ae (Wael Zaki), claire.morin@emse.fr (Claire Morin), ziad.moumni@ensta-paristech.fr (Ziad Moumni), zhangwh@nwpu.edu.cn (Weihong Zhang)

Keywords: shape memory alloys; nonproportional loading; multiaxial loading; phase transformation; martensite reorientation; multisurface inelasticity.

1. Introduction

Shape memory alloys (SMAs) are capable of sustaining severe inelastic deformation that can be recovered by heating (Otsuka and Wayman, 1999). This behavior is explained by the ability of SMAs to undergo transformation between a higher symmetry austenite phase and a lower symmetry martensite phase. The martensite phase can be inelastically deformed by detwinning and reorientation of variants characterized by different crystallographic orientations (Funakubo, 1987). Starting from the 1970's, the use of SMAs in engineering applications has seen significant development (Humbeeck, 1999) and it now spans a number of important fields ranging from biomedicine to civil engineering and aeronautics (Stöckel, 2001). A key feature of many shape memory alloys is superelasticity, which refers to the capacity of these materials to undergo substantial deformation when subjected to mechanical loading at temperatures exceeding the so-called “austenite finish” temperature and to recover their undeformed shape once the load is removed. Finite element analysis of this superelastic behavior in cases of uniaxial and multiaxial proportional and nonproportional isothermal loading is the focus of this paper.

Uniaxial or multiaxial loading of shape memory alloys can induce phase transformation accompanied by the nucleation or shrinking of martensite variants (Otsuka and Wayman, 1999; Bodaghi et al., 2013). When the loading direction changes, preferred martensite variants begin to form at the

expense of others leading to a change in orientation of the inelastic strain in the martensitic phase. Both phase change and martensite reorientation can take place at the same time in presence of multiaxial nonproportional loading, which motivates the need for SMA models capable of accounting for these processes simultaneously. Numerical integration of the constitutive equations in this case is particularly challenging because it typically involves solving highly nonlinear equations while satisfying multiple consistency conditions and intrinsic constraints on the state variables. Proper numerical integration of SMA models is of special importance in such areas as the mechanics of fracture of SMAs, where multiaxial loading conditions and severe stress gradients are experienced by the material in the neighbourhood of the crack tip, as well as in analyzing fatigue of SMA structures, where accurate simulation of the multiaxial behavior of the material is needed for numerical prediction of fatigue life using appropriate failure criteria.

In the literature, the behavior of SMAs subjected to nonproportional loading has been the subject of intense investigation. Sittner et al. (1995) performed biaxial tension-torsion experiments on polycrystalline CuAlZnMn SMA samples considering rectangular and triangular stress- and strain-controlled loading cases. In both cases, the inelastic deformation of the material was found to be fully recoverable by unloading. Lim and McDowell (1999) reported several biaxial proportional and nonproportional loading experiments for thin-wall tubes of superelastic NiTi SMAs under circular normal/shear stress- and strain-controlled loading. The material response was found to exhibit tensile-compressive asymmetry when subjected to cyclic tensile-compressive loading. Moreover, force- and strain-controlled experiments were conducted at different strain rates, with and without hold times, and the results were reported including the influence of thermomechanical

coupling. Bouvet et al. (2002) carried out tension/internal pressure tests and biaxial compression tests using CuAlBe SMA samples where the authors also observed tensile compressive asymmetry in the material behavior. A model was later proposed (Bouvet et al., 2004) that takes into account this asymmetry, as well as the influence of temperature, return point memory and the nonproportionality of the applied load on SMA behavior. The model was validated against experimental data obtained under general multi-axial loading cases. Panico and Brinson (2007) proposed a macroscopic phenomenological model based on the framework of thermodynamics of irreversible processes. The model accounts for the influence of multi-axial stress states and non-proportional loading histories and was shown to reasonably agree with the experimental data in (Sittner et al., 1995). Grabe and Bruhns (2009) reported experimental results for polycrystalline NiTi subjected to several multi-axial loading cases in a wide temperature range in order to investigate superelasticity and the one-way shape memory effect of the material. Based on these experiments, the use of von Mises equivalent stress in deriving loading functions for phase transformation and martensite reorientation was found inappropriate as it failed to capture tensile-compressive and tensile-torsional asymmetries. Arghavani et al. (2010) presented a phenomenological constitutive model that accounts for key features of SMA behavior when the material is subjected to proportional as well as non-proportional loading. The model was successfully used to simulate a number of experimental results taken from the literature. (Chemisky et al., 2011) derived a model for shape memory alloys based on earlier work by the authors. The model focuses on SMA behavior at lower stress levels and takes into account several effects associated with SMA behavior such as tensile-compressive asymmetry and temperature-driven phase transfor-

mation. Simulation results are reported, without validation, at different temperatures for a case of multiaxial loading consisting of a square tension-shear loading path. Another model was developed by Stebner and Brinson (2013). The model was numerically integrated using an explicit scheme. Care was taken in eliminating the need for user-calibration of the numerical integration parameters and reducing the sensitivity of the integration algorithm to mass scaling for faster computation. Bodaghi et al. (2013) derived a simple and robust phenomenological model for SMAs using the framework of continuum thermodynamics of irreversible processes. The model was used to simulate SMAs subjected to uniaxial and biaxial loading, including proportional and nonproportional tensile-torsional loading. Good agreement with experimental data was achieved for these loading cases. Auricchio et al. (2014) recently proposed a model for SMAs that accounts for several aspects of SMA behavior in presence of multiaxial loading. The model was numerically integrated using Fischer-Burmeister functions to account for the Kuhn-Tucker conditions governing the evolution of several state variables, including the volume fractions of single- and multi-variant martensites and the directional orientation of single-variant martensite. The use of the Fischer-Burmeister functions allowed the authors to dispense with the conventional search for active loading surfaces by substituting the Kuhn-Tucker inequalities with a set of equivalent nonlinear equalities. The model is validated against experimental data for several loading cases, including a case of combined tension-torsion involving a helical SMA spring. A recent model was also proposed by Mehrabi et al. (2014), which consisted of a thermodynamically acceptable evolution of the microplane model for SMAs. In the spirit of the microplane theory, the authors considered different stress projection methods to resolve the three-dimensional constitutive material behavior

into a combination of uniaxial models defined in specific spatial directions. The model was then used to simulate experiments on a thin hollow SMA cylinder subjected to tension, torsion and combined tension-torsion loading cases. Only proportional loading was considered for the combined loading case

Zaki and Moumni (2007b,a) and Moumni et al. (2008) derived a phenomenological model that can simultaneously account for phase transformation and martensite detwinning and reorientation. The model was improved to account for tensile-compressive asymmetry (Zaki et al., 2011; Zaki, 2010), plastic yielding (Zaki et al., 2010), and thermomechanical coupling (Morin et al., 2011a) including cyclic effects (Morin et al., 2011b; Moumni et al., 2009; Morin et al., 2011c; Morin, 2011). However, numerical integration of the model in presence of non-proportional multiaxial loading was only considered so far in the case of martensitic SMAs (Zaki, 2012a,b).

This paper presents detailed integration for the Zaki-Moumni (ZM) model for SMAs capable of undergoing combined phase transformation and martensite reorientation when subjected to nonproportional multiaxial loading. Proper numerical integration and extensive validation of the model for such general loading cases has not been attempted before and therefore constitutes the novelty of this work. The implicit time integration procedure is implemented by means of a user material subroutine into the finite element software Abaqus.

The paper provides a brief review of the ZM models in section 2 followed by a general presentation of the boundary value problem and time-discrete equations for a SMA subjected to isothermal loading in section 3, including a closed-form expression for the continuous material Jacobian. Numerical simulations are then carried out in section 4 for a number of loading cases,

many of which are taken from the literature and shown to be properly simulated by the model. A general conclusion and outlook are finally provided in section 5.

2. Summary of the analytical model

The ZM model for shape memory materials is developed based on the framework of generalized standard materials (Halphen and Nguyen, 1974) that was slightly extended to account for constraints on the state variables (Moumni, 1995; Moumni et al., 2008). Using standard index notation for tensor representation and implied summation over repeated indices, the derivation of the model gives the following stress-strain relation:

$$\sigma_{ij} = K_{ijkl}(\varepsilon_{kl} - z\varepsilon_{kl}^{ori}) \quad (1)$$

where σ_{ij} and ε_{kl} are the stress and total strain tensors, z is the volume fraction of martensite and ε_{kl}^{ori} is the inelastic strain caused by martensite detwinning and reorientation. The elastic stiffness tensor K_{ijkl} is a function of phase composition. It is given by the expression

$$K_{ijkl} = \left[(1-z)K_{ijkl}^{A,-1} + zK_{ijkl}^{M,-1} \right]^{-1}, \quad (2)$$

in which K_{ijkl}^A and K_{ijkl}^M are the elastic stiffness matrices of austenite and martensite respectively.

The volume fraction of martensite cannot be less than zero or greater than one and the recoverable inelastic deformation of martensite is limited by a maximum ε_0 that depends on the material used. These constraints are mathematically expressed as

$$z \geq 0, \quad 1 - z \geq 0, \quad \text{and} \quad \varepsilon_0 - \varepsilon_{eq}^{ori} \geq 0 \quad (3)$$

where ε_{eq}^{ori} is an equivalent orientation strain taken in this paper to be

$$\varepsilon_{eq}^{ori} = \sqrt{\frac{2}{3}\varepsilon_{ij}^{ori}\varepsilon_{ij}^{ori}}. \quad (4)$$

The evolution of the dissipative variables z and ε_{ij}^{ori} is governed by the Kuhn-Tucker conditions

$$\mathcal{F}_z^1(\sigma_{ij}, z, \varepsilon_{ij}^{ori}) \leq 0, \quad \dot{z} \geq 0, \quad \dot{z}\mathcal{F}_z^1 = 0, \quad (5)$$

for forward transformation, in which $0 \leq z < 1$;

$$\mathcal{F}_z^2(\sigma_{ij}, z, \varepsilon_{ij}^{ori}) \leq 0, \quad -\dot{z} \geq 0, \quad -\dot{z}\mathcal{F}_z^2 = 0, \quad (6)$$

for reverse transformation, in which $0 < z \leq 1$;

$$\mathcal{F}_{ori}(\sigma_{ij}, z, \varepsilon_{ij}^{ori}) \leq 0, \quad \eta \geq 0, \quad \eta\mathcal{F}_{ori} = 0, \quad (7)$$

for martensite detwinning and reorientation, in which η is the inelastic multiplier and the rate of orientation strain is provided by the normality rule

$$\dot{\varepsilon}_{ij}^{ori} = \eta \frac{\partial \mathcal{F}_{ori}}{\partial X_{ij}} = \frac{3}{2}\eta \frac{X_{ij}}{X_{vm}} = \eta N_{ij}. \quad (8)$$

In the above equation, X_{vm} is the von Mises equivalent of the thermodynamic force X_{ij} , conjugate to the orientation strain ε_{ij}^{ori} , and $N_{ij} = \frac{3}{2}\frac{X_{ij}}{X_{vm}}$ is a vector indicating the direction of the orientation strain rate $\dot{\varepsilon}_{ij}^{ori}$ in strain space. To simplify numerical integration, martensite is assumed to be fully oriented by the applied stress as soon as the phase transformation from austenite to martensite takes place. This simplification is in accordance with results in the literature (Patoor et al., 2006). For the ZM model used, this assumption is equivalent to considering that the stress σ_{rf} needed for complete detwinning of martensite is less than the stress σ_{ms} required to initiate forward phase transformation.

3. Boundary value problem and algorithmic setup

3.1. Boundary value problem

A superelastic SMA structure occupying a volume $\Omega \in \mathbb{R}^3$ is subjected to isothermal loading in the time interval $[0, T]$. The load consists of body forces $f_i(x, t)$ acting over $\Omega \times [0, T]$ and contact forces $T_i^d(x, t)$ acting over $\partial\Omega_T \times [0, T]$. Displacement is constrained over the remaining boundary $\partial\Omega_\xi$ in the time interval $[0, T]$. Starting from an initial configuration at time $t = 0$ in which the state variables are known and using the subscript notation $_{,i}$ to indicate differentiation with respect to space coordinate i , the problem consists in solving the following set of equations over Ω for $t \in [0, T]$:

- Static equilibrium

$$\begin{aligned} \sigma_{ij,j} + f_i &= 0 && \text{in } \Omega, \\ \sigma_{ij}n_j &= T_i^d && \text{over } \partial\Omega_T, \end{aligned} \tag{9}$$

where n_j is an outward unit vector normal to the boundary $\partial\Omega_T$,

- Kinematic boundary conditions

$$\xi_i = \xi_i^d \text{ over } \partial\Omega_\xi, \tag{10}$$

where ξ_i is the displacement vector,

- Strain compatibility

$$\varepsilon_{ij} = \frac{1}{2} (\xi_{i,j} + \xi_{j,i}) \text{ in } \Omega, \tag{11}$$

- Constitutive equations

$$\sigma_{ij} = K_{ijkl} (\varepsilon_{kl} - z\varepsilon_{kl}^{ori}) \text{ in } \Omega \tag{12}$$

where K_{ijkl} is given by (2), and z and ε_{ij}^{ori} are governed by the conditions (3) to (8).

The boundary value problem above is solved using the finite element method. Time integration of the constitutive equations is done using an implicit algorithm that takes into account the possibility of simultaneous phase transformation and martensite detwinning and reorientation in presence of nonproportional multiaxial loading.

The assumption of complete orientation of martensite as soon as it forms reduces the constraint on the orientation strain to the equality $\varepsilon_0 - \varepsilon_{eq}^{ori} = 0$. The loading function \mathcal{F}_{ori} governing the orientation of martensite can be written in this case as

$$\mathcal{F}_{ori} = X_{vm} - zY \text{ where } X_{ij} = s_{ij} - \frac{2}{3\varepsilon_0^2} (s_{kl}\varepsilon_{kl}^{ori}) \varepsilon_{ij}^{ori}, \quad (13)$$

in which s_{ij} is the stress deviator and Y is a material parameter that defines the stress onset of martensite detwinning in uniaxial tension. The expressions of the phase transformation functions remain unchanged with respect to the original ZM model. They are given by

$$\begin{aligned} \mathcal{F}_z^1 &= \frac{1}{2} \left(\frac{3}{2} El_{MA} s_{ij} s_{ij} + P_{MA} \sigma_{ii}^2 \right) - C(T) \\ &\quad + s_{ij} \varepsilon_{ij}^{ori} - (G + b)z - a(1 - z) \\ &\quad - \left[(\alpha - \beta)z + \frac{\beta}{2} \right] \left(\frac{2}{3} \varepsilon_{ij}^{ori} \varepsilon_{ij}^{ori} \right), \end{aligned} \quad (14)$$

$$\begin{aligned} \mathcal{F}_z^2 &= -\frac{1}{2} \left(\frac{3}{2} El_{MA} s_{ij} s_{ij} + P_{MA} \sigma_{ii}^2 \right) + C(T) \\ &\quad - s_{ij} \varepsilon_{ij}^{ori} + (G - b)z - a(1 - z) \\ &\quad + \left[(\alpha - \beta)z + \frac{\beta}{2} \right] \left(\frac{2}{3} \varepsilon_{ij}^{ori} \varepsilon_{ij}^{ori} \right), \end{aligned} \quad (15)$$

where El_{MA} , P_{MA} , α , β , a , b , G are material parameters and $C(T)$ is a function of temperature.

Considering a discretization of the time interval $[0, T]$ into N intervals, the increments of the state variables z and ε_{ij}^{ori} for load increment $n + 1$, $n \in$

$\{0, N\}$, are determined by enforcing the appropriate consistency conditions assuming z and ε_{ij}^{ori} are known at load increment n . In the equations below, the load increments n and $n + 1$ are indicated in the subscript and the solution iteration k is indicated in the superscript of the relevant variable. The incremental equations are solved using a classical predictor-corrector strategy (Simo and Hughes, 1998) as follows:

- An elastic stress increment is first determined that achieves static equilibrium:

$$z_{n+1}^{(0)} = z_n \text{ and } \varepsilon_{ij,n+1}^{ori,(0)} = \varepsilon_{ij,n}^{ori} \quad (16)$$

$$\sigma_{ij,n+1}^{(0)} = K_{ijkl,n+1}^{(0)} \left(\varepsilon_{kl,n+1} - z_{n+1}^{(0)} \varepsilon_{kl,n+1}^{ori,(0)} \right) \quad (17)$$

- The stress increment is then corrected and the state variables are updated in accordance with the consistency conditions. If \mathcal{F}_z is any of the two loading functions \mathcal{F}_z^1 and \mathcal{F}_z^2 governing phase change, these conditions must satisfy

$$\mathcal{F}_z \left(\sigma_{ij}^{(k)}, z^{(k)}, \varepsilon_{ij}^{ori,(k)} \right) \leq 0 \quad (18)$$

$$\mathcal{F}_{ori} \left(\sigma_{ij}^{(k)}, z^{(k)}, \varepsilon_{ij}^{ori,(k)} \right) \leq 0 \quad (19)$$

where the subscript $n + 1$ is eliminated for readability and where each inequality reduces to a strict equality when the relevant process is active. The equalities can be approximated using first-order Taylor series expansions of the loading functions \mathcal{F}_z and \mathcal{F}_{ori} in the neighbourhood of $\left(\sigma_{ij}^{(k-1)}, z^{(k-1)}, \varepsilon_{ij}^{ori,(k-1)} \right)$, which can then be solved iteratively. The Taylor

series approximations are written explicitly as follows:

$$\begin{aligned} \mathcal{F}_z^{(k-1)} + \frac{\partial \mathcal{F}_z^{(k-1)}}{\partial \sigma_{ij}} \Delta \sigma_{ij}^{(k)} \\ + \frac{\partial \mathcal{F}_z^{(k-1)}}{\partial z} \Delta z^{(k)} + \frac{\partial \mathcal{F}_z^{(k-1)}}{\partial \varepsilon_{ij}^{ori}} \Delta \varepsilon_{ij}^{ori,(k)} = 0 \end{aligned} \quad (20)$$

$$\begin{aligned} \mathcal{F}_{ori}^{(k-1)} + \frac{\partial \mathcal{F}_{ori}^{(k-1)}}{\partial \sigma_{ij}} \Delta \sigma_{ij}^{(k)} \\ + \frac{\partial \mathcal{F}_{ori}^{(k-1)}}{\partial z} \Delta z^{(k)} + \frac{\partial \mathcal{F}_{ori}^{(k-1)}}{\partial \varepsilon_{ij}^{ori}} \Delta \varepsilon_{ij}^{ori,(k)} = 0 \end{aligned} \quad (21)$$

where $\Delta v^{(k)} = v^{(k)} - v^{(k-1)}$ is the increment of variable v at iteration k . If phase transformation and martensite orientation are active at the same time, $\Delta z^{(k)}$ and $\eta^{(k)}$ are obtained by solving the time-discrete equations (20) and (21) simultaneously, where $\eta^{(k)}$ is the discrete inelastic multiplier used to express the discrete normality rule at iteration k as

$$\Delta \varepsilon_{ij}^{ori,(k)} = \eta^{(k)} N_{ij}^{(k)}. \quad (22)$$

N_{ij} in the previous equation is approximated at iteration k by its value at the previous iteration, with the initial value corresponding to an elastic prediction. Substituting (22) into (20) and (21) gives

$$\begin{aligned} \mathcal{F}_z^{(k-1)} + \frac{\partial \mathcal{F}_z^{(k-1)}}{\partial \sigma_{ij}} \Delta \sigma_{ij}^{(k)} + \frac{\partial \mathcal{F}_z^{(k-1)}}{\partial z} \Delta z^{(k)} \\ + \eta^{(k)} \frac{\partial \mathcal{F}_z^{(k-1)}}{\partial \varepsilon_{ij}^{ori}} N_{ij}^{(k)} = 0, \end{aligned} \quad (23)$$

$$\begin{aligned} \mathcal{F}_{ori}^{(k-1)} + \frac{\partial \mathcal{F}_{ori}^{(k-1)}}{\partial \sigma_{ij}} \Delta \sigma_{ij}^{(k)} + \frac{\partial \mathcal{F}_{ori}^{(k-1)}}{\partial z} \Delta z^{(k)} \\ + \eta^{(k)} \frac{\partial \mathcal{F}_{ori}^{(k-1)}}{\partial \varepsilon_{ij}^{ori}} N_{ij}^{(k)} = 0. \end{aligned} \quad (24)$$

The time-discrete stress-strain relation can then be written as

$$\Delta\sigma_{ij}^{(k)} = K_{ijkl}^{(k-1)} \left[\Delta\varepsilon_{kl}^{(k)} - \left(\Delta K_{ijkl}^{-1,(k)} \sigma_{ij}^{(k-1)} + \Delta z^{(k)} \varepsilon_{kl}^{ori,(k-1)} + z^{(k-1)} \Delta\varepsilon_{kl}^{ori,(k)} \right) \right] \quad (25)$$

where $\Delta\varepsilon_{kl}^{(k)} = 0$ because ε_{ij} is not updated in the corrector step and the increment of the elastic compliance tensor is given by

$$\Delta K_{ijkl}^{-1,(k)} = \left(K_{ijkl}^{M,-1} - K_{ijkl}^{A,-1} \right) \Delta z^{(k)}. \quad (26)$$

Combining equations (22), (25) and (26) gives

$$\Delta\sigma_{ij}^{(k)} = -K_{ijkl}^{(k-1)} \left[R_{kl}^{(k-1)} \Delta z^{(k)} + z^{(k-1)} \eta^{(k)} N_{kl}^{(k)} \right] \quad (27)$$

where

$$R_{kl}^{(k-1)} = \left(K_{ijkl}^{M,-1} - K_{ijkl}^{A,-1} \right) \sigma_{ij}^{(k-1)} + \varepsilon_{kl}^{ori,(k-1)} \quad (28)$$

The increments of the martensite volume fraction $\Delta z^{(k)}$ and the multiplier $\eta^{(k)}$ can now be calculated as

$$\Delta z^{(k)} = \frac{A_{ori}^{(k)} \mathcal{F}_{ori}^{(k-1)} - B_{ori}^{(k)} \mathcal{F}_z^{(k-1)}}{A_z^{(k)} B_{ori}^{(k)} - B_z^{(k)} A_{ori}^{(k)}}, \quad (29)$$

$$\eta^{(k)} = \frac{B_z^{(k)} \mathcal{F}_z^{(k-1)} - A_z^{(k)} \mathcal{F}_{ori}^{(k-1)}}{A_z^{(k)} B_{ori}^{(k)} - B_z^{(k)} A_{ori}^{(k)}}, \quad (30)$$

where

$$A_z^{(k)} = \frac{\partial \mathcal{F}_z^{(k-1)}}{\partial z} - K_{ijkl}^{(k-1)} \frac{\partial \mathcal{F}_z^{(k-1)}}{\partial \sigma_{ij}} R_{kl}^{(k-1)}, \quad (31)$$

$$A_{ori}^{(k)} = \frac{\partial \mathcal{F}_z^{(k-1)}}{\partial \varepsilon_{ij}^{ori}} N_{ij}^{(k)} - z^{(k-1)} K_{ijkl}^{(k-1)} \frac{\partial \mathcal{F}_z^{(k-1)}}{\partial \sigma_{ij}} N_{kl}^{(k)}, \quad (32)$$

$$B_z^{(k)} = \frac{\partial \mathcal{F}_{ori}^{(k-1)}}{\partial z} - K_{ijkl}^{(k-1)} \frac{\partial \mathcal{F}_{ori}^{(k-1)}}{\partial \sigma_{ij}} R_{kl}^{(k-1)}, \quad (33)$$

$$B_{ori}^{(k)} = \frac{\partial \mathcal{F}_{ori}^{(k-1)}}{\partial \varepsilon_{ij}^{ori}} N_{ij}^{(k)} - z^{(k-1)} K_{ijkl}^{(k-1)} \frac{\partial \mathcal{F}_{ori}^{(k-1)}}{\partial \sigma_{ij}} N_{kl}^{(k)}, \quad (34)$$

For phase transformation without martensite reorientation, the increment of martensite volume fraction at iteration k is given by the simple equation

$$\Delta z^{(k)} = -\frac{\mathcal{F}_z^{(k-1)}}{A_z^{(k)}}. \quad (35)$$

Similarly, the inelastic multiplier at iteration k in the case of martensite reorientation without phase transformation is given by

$$\eta^{(k)} = -\frac{\mathcal{F}_{ori}^{(k-1)}}{B_{ori}^{(k)}} \quad (36)$$

3.2. Derivation of a continuous material Jacobian

For small volume changes, the continuous material Jacobian at the beginning of increment $n + 1$ is given by

$$\mathcal{J}_{ijkl} = \frac{d\sigma_{ij}}{d\varepsilon_{kl}} \quad (37)$$

where the right-hand term is evaluated at the end of increment n .

The time-continuous stress-strain relation can be written in differential form as

$$d\sigma_{ij} = K_{ijkl} [d\varepsilon_{kl} - (R_{kl}dz + \eta z N_{kl})] \quad (38)$$

For combined phase transformation and martensite reorientation, substituting dz and η in the above with the expressions

$$dz = \frac{A_{ori}K_{ijkl}\frac{\partial\mathcal{F}_{ori}}{\partial\sigma_{ij}} - B_{ori}K_{ijkl}\frac{\partial\mathcal{F}_z}{\partial\sigma_{ij}}}{A_zB_{ori} - B_zA_{ori}}d\varepsilon_{kl}, \quad (39)$$

$$\eta = \frac{B_zK_{ijkl}\frac{\partial\mathcal{F}_z}{\partial\sigma_{ij}} - A_zK_{ijkl}\frac{\partial\mathcal{F}_{ori}}{\partial\sigma_{ij}}}{A_zB_{ori} - B_zA_{ori}}d\varepsilon_{kl}, \quad (40)$$

leads to the following closed-form expression of the continuous material Jacobian:

$$\begin{aligned}
\mathcal{J}_{ijkl} &= \frac{d\sigma_{ij}}{d\varepsilon_{kl}} \\
&= K_{ijkl} - K_{ijpq}R_{pq} \frac{A_{ori}K_{rskl} \frac{\partial \mathcal{F}_{ori}}{\partial \sigma_{rs}} - B_{ori}K_{rskl} \frac{\partial \mathcal{F}_z}{\partial \sigma_{rs}}}{A_z B_{ori} - B_z A_{ori}} \\
&\quad - zK_{ijpq}N_{pq} \frac{B_z K_{rskl} \frac{\partial \mathcal{F}_z}{\partial \sigma_{rs}} - A_z K_{ijrs} \frac{\partial \mathcal{F}_{ori}}{\partial \sigma_{rs}}}{A_z B_{ori} - B_z A_{ori}}
\end{aligned} \tag{41}$$

The same procedure gives the following expressions of the material Jacobian for the case of phase transformation with no reorientation of martensite and for the case of martensite reorientation without phase transformation:

$$\mathcal{J}_{ijkl} = \frac{d\sigma_{ij}}{d\varepsilon_{kl}} = K_{ijkl} - K_{ijpq}R_{pq} \frac{K_{rskl} \frac{\partial \mathcal{F}_z}{\partial \sigma_{rs}}}{A_z} \tag{42}$$

and

$$\mathcal{J}_{ijkl} = \frac{d\sigma_{ij}}{d\varepsilon_{kl}} = K_{ijkl} - zK_{ijpq}N_{pq} \frac{K_{rskl} \frac{\partial \mathcal{F}_{ori}}{\partial \sigma_{rs}}}{B_{ori}} \tag{43}$$

respectively.

3.3. Algorithmic setup

A ‘‘User Material’’ subroutine is developed for the simulation of phase transformation and martensite reorientation in the finite element analysis software Abaqus. The subroutine uses the implicit integration algorithm presented below in order to update the stress components and the state variables at the end of each load increment.

1. Read the parameters of the model,
2. Determine the elastic trial state:
 - Calculate the increment of trial stress $\sigma_{ij,n+1}^{(0)}$ using (17),

- Calculate initial trial values for the loading functions $\mathcal{F}_{z,n+1}^{(0)}, \mathcal{F}_{ori,n+1}^{(0)}$;
3. If $\mathcal{F}_{z,n+1}^{(0)} \leq 0$ and $\mathcal{F}_{ori,n+1}^{(0)} \leq 0$, the trial solution is acceptable:
 - Set the stress vector equal to the trial stress vector,
 - Set the state variables to their values at the beginning of the increment,
 - Set the material Jacobian \mathcal{J}_{ijkl} equal to the elastic stiffness tensor K_{ijkl} ;
 4. Else if $\mathcal{F}_{z,n+1}^{(0)} \leq 0$ and $\mathcal{F}_{ori,n+1}^{(0)} > 0$, (only martensite reorientation is active):
 - Calculate the increment of the inelastic multiplier η_{n+1} using (30)
 - Update the state variables,
 - Calculate the material Jacobian \mathcal{J}_{ijkl} using (43);
 5. Else if $\mathcal{F}_{z,n+1}^{(0)} > 0, \mathcal{F}_{ori,n+1}^{(0)} \leq 0$ (only phase transformation is active):
 - Calculate the increment of martensite volume fraction Δz_{n+1} using (29),
 - Update the state variables,
 - Calculate the material Jacobian \mathcal{J}_{ijkl} using (42);
 6. Else if $\mathcal{F}_{z,n+1}^{(0)} > 0$ and $\mathcal{F}_{ori,n+1}^{(0)} > 0$ (martensite reorientation *or* phase transformation *or* both):
 - Calculate the increment of the inelastic multiplier η_{n+1} and the increment of martensite volume fraction Δz_{n+1} using (29) and (30),
 - (a) If ($\Delta z_{n+1} > 0$ and $\mathcal{F}_{z,n+1}^{1,(0)} > 0$ and $\eta_{n+1} > 0$) *or* ($\Delta z < 0$ and $\mathcal{F}_{z,n+1}^{2,(0)} > 0$ and $\eta_{n+1} > 0$), then (simultaneous phase transformation and martensite reorientation):

- Update the stress vector and the state variables,
 - Calculate the material Jacobian \mathcal{J}_{ijkl} using Eq.(41);
- (b) Else if ($\Delta z_{n+1} < 0$ and $\mathcal{F}_{z,n+1}^{1,(0)} > 0$ and $\eta_{n+1} > 0$) or ($\Delta z_{n+1} > 0$ and $\mathcal{F}_{z,n+1}^{2,(0)} > 0$ and $\eta_{n+1} > 0$), then (martensite reorientation only):
- Reset the state variables to their values at the beginning of the increment,
 - Calculate the inelastic multiplier η_{n+1} using (30),
 - Update the state variables,
 - Calculate the material Jacobian \mathcal{J}_{ijkl} using (43);
- (c) Else if ($\Delta z_{n+1} > 0$ and $\mathcal{F}_{z,n+1}^{1,(0)} > 0$ and $\eta_{n+1} < 0$) or ($\Delta z < 0$ and $\mathcal{F}_{z,n+1}^{2,(0)} > 0$ and $\eta_{n+1} < 0$), then (phase transformation only):
- Reset the state variables to their values at the beginning of the increment,
 - Calculate the increment of martensite volume fraction Δz_{n+1} using (29),
 - Update the state variables,
 - Calculate the material Jacobian \mathcal{J}_{ijkl} using (42).

4. Results and discussions

The problem defined in the previous section is solved by means of the finite element method for several superelastic SMA structures subjected to uniaxial and multiaxial proportional and nonproportional loading. The section is organized as follows:

- Proportional loading is considered in section 4.1, which includes numerical simulation results for pure tension, pure torsion, as well as multiaxial tension-torsion and tension-internal pressure loading that are compared to experimental data from Bouvet et al. (2004).
- A hypothetical situation involving nonproportional loading is presented in section 4.2 in order to investigate the ability of the model to account for multiaxial loading in presence of simultaneous phase transformation and martensite reorientation.
- In section 4.3, the model is used to simulate a number of numerical as well as experimental results available in the literature for SMAs subjected to nonproportional multiaxial loading. The reference data used for the validation are those reported by Sittner et al. (1995), Bouvet et al. (2002), Stebner and Brinson (2013), Panico and Brinson (2007), Arghavani et al. (2010), Grabe and Bruhns (2009). In each case, the parameters used for the simulations using the ZM model were obtained by curve fitting to a subset of the reported data.

4.1. Simulation of proportional loading cases

The four loading cases shown in figure 1 are considered in this section, ranging from pure tension (path 1) to pure shear (path 2). Paths 3 and 4 represent combined tensile-shear loading where tension is dominant for path 3 and shear is dominant for path 4.

The simulations are performed on a single 8-node hexahedral element with reduced integration. A maximum von Mises equivalent stress of 800 MPa is achieved in each loading case and a constant temperature $T = 340 \text{ K}$ is considered for which the shape memory alloy is superelastic. The parameters

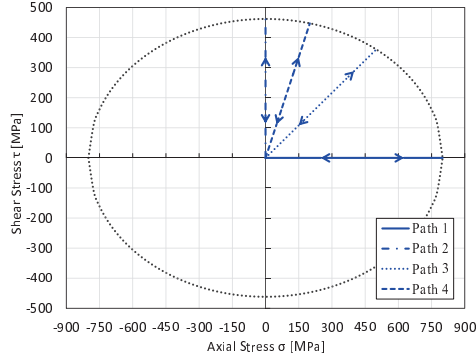


Figure 1: Stress-controlled proportional loading cases.

used for the simulations are listed in table 1.

Parameter	Value	Parameter	Value
E_A	30340 MPa	a	5.16 MPa
E_M	18000 MPa	b	6.36 MPa
ν	0.3	ε_0	0.04
Y	30 MPa	G	13.17 MPa
α	500 MPa	β	1250 MPa
ξ	0.20 MPa	κ	4.16 MPa
A_f^0	300 K	T	340 K

Table 1: Material Parameters used for the finite element simulations in section 4.1

The simulated uniaxial response of the material is shown in figures 2(a) for tensile loading and 2(b) for shear loading. The obtained superelastic loops are identical in shape up to a scaling factor of $\sqrt{3}$ along the coordinate axes.

Simulation results for the combined loading cases corresponding to the loading paths 3 and 4 on figure 1 are shown in figures 3 and 4. In both

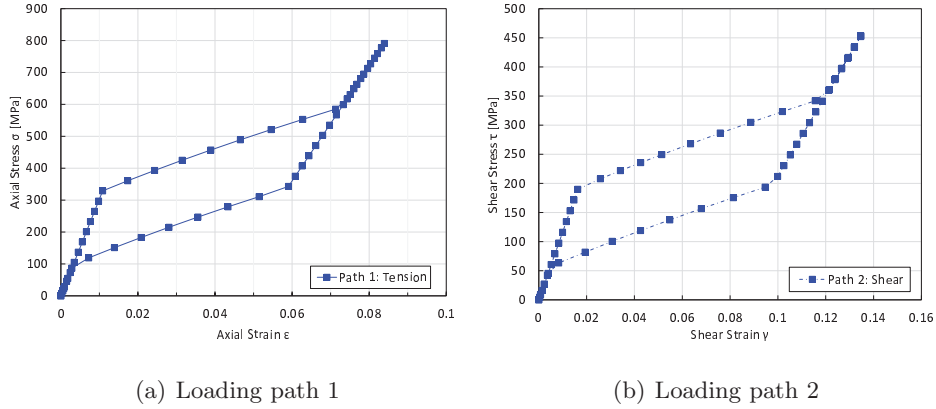


Figure 2: Simulated stress-strain behavior for pure tension and pure shear loading.

cases, tensile and shear superelasticity is obtained with full inelastic strain recovery when the load is removed.

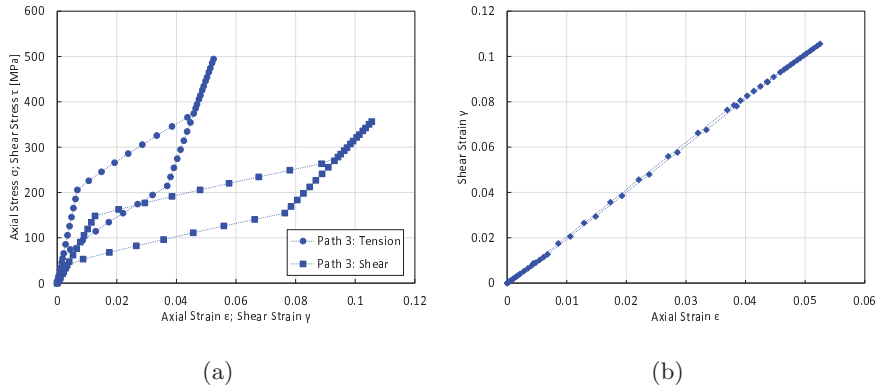


Figure 3: Simulated stress-strain behavior and shear versus axial strain for tension-dominated tensile-shear loading (loading path 3).

The model is now used to simulate the behavior of a thin-wall SMA cylinder following Bouvet et al. (2004). The cylinder is subjected to proportional multiaxial loading consisting of a combination of axial loading and internal pressure. The material parameters used for the simulation are reported in table 2.

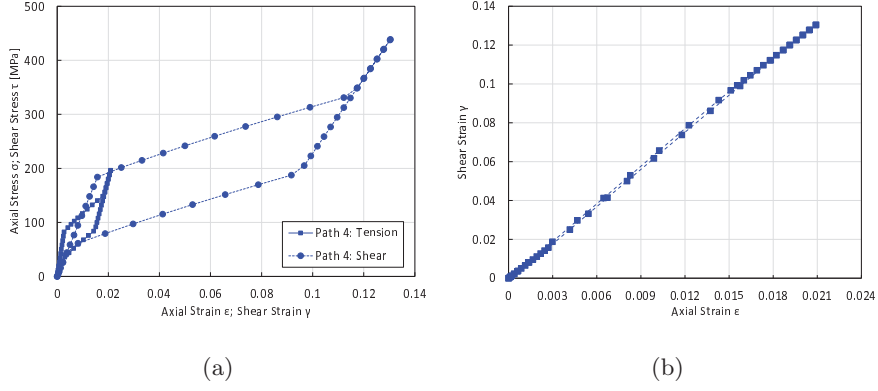


Figure 4: Simulated stress-strain behavior and shear versus axial strain for shear-dominated tensile-shear loading (loading path 4).

Parameter	Value	Parameter	Value
E_A	45200 MPa	a	0.24 MPa
E_M	26400 MPa	b	0.096 MPa
ν	0.3	ϵ_0	0.008
Y	30 MPa	G	1.92 MPa
α	2500 MPa	β	6250 MPa
ξ	0.0145 MPa	κ	0.038 MPa
A_f^0	300 K	T	340 K

Table 2: material parameters obtained using data form Bouvet et al.(2004).

The loading considered in this case corresponds to the hoop versus axial stress shown in figure 5, in which a constant slope is obtained because of the proportional nature of the load.

The resulting stress-strain behavior of the material is shown in figure 6 where two superelastic stress-strain loops are shown representing the material behavior in the axial and hoop directions respectively. The simulations are in good agreement with the experimental data in both cases. In particular,

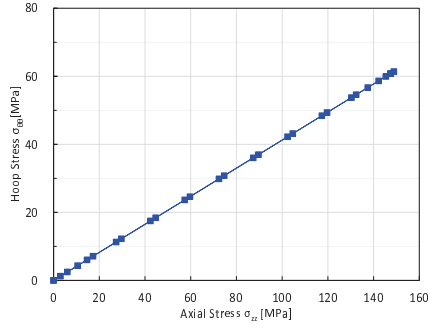


Figure 5: Proportional tension-internal pressure loading.

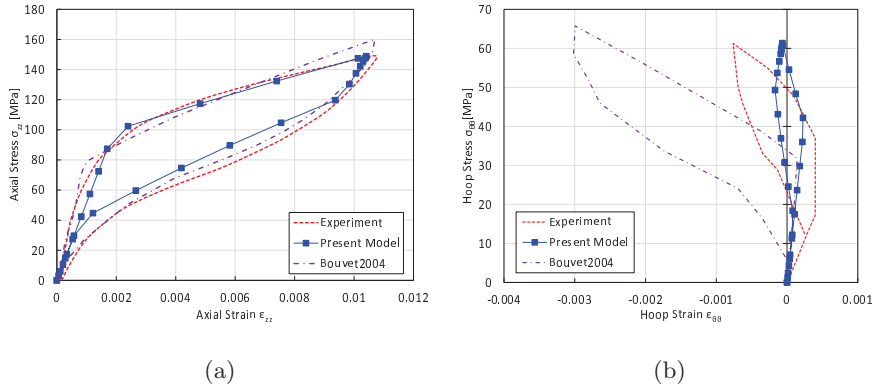


Figure 6: Stress-strain behavior of the SMA in the axial and hoop directions

the model provides improved prediction of the material behavior in the hoop direction. Deviation from the experimental data may be due to a number of reasons, including the use of von Mises equivalent stress in the present version of the model, which cannot reproduce potential asymmetry in the material response.

4.2. Multiaxial reorientation tests

A preliminary numerical simulation test is performed in this section in order to illustrate the ability of the model to simulate simultaneous phase transformation and martensite reorientation and to account for martensite

reorientation at saturation, in which case the equivalent orientation strain reaches its maximum value ε_0 . In case the loading magnitude continues to increase beyond the saturation point, the components of the orientation strain tensor ε_{ij}^{ori} may continue to evolve to accommodate possible modifications in the loading direction while the equivalent orientation strain remains constant.

The parameters used in this section are those listed in table 1. The proposed simulation involves an axial loading corresponding to a maximum normal stress of 450 MPa followed by an increase in shear stress from 0 to 200 MPa as shown in figure 7(a). The maximum normal stress is such that maximum inelastic strain is achieved in tension (complete transformation of austenite to fully oriented martensite) as shown in figure 7(b). The superposition of shear stress leads to an increase in the yz strain component at the expense of the normal xx strain in such way that the total equivalent orientation strain remains constant (same figure). The evolution of the inelastic strain components is an expression of the physical process of martensite reorientation, in which preferred martensite variants form at the expense of other variants that are less-favorably oriented with respect to the applied load. From a phenomenological point of view, within the frame of the ZM model for shape memory alloys, this behavior is captured through the use of the loading function for martensite orientation \mathcal{F}_{ori} .

Further testing of the model is carried out using the square loading path shown in figure 8(a), which consists of the following loading steps starting from an unloaded state:

1. Tensile loading up to a maximum tensile stress of 250 MPa (segment AB on the figure),

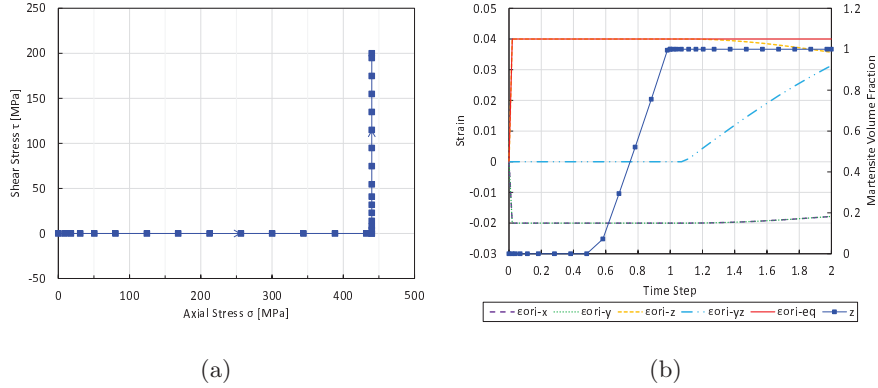


Figure 7: Simulation of martensite reorientation under multiaxial loading: (a) axial-shear loading path; (b) evolution of the martensite volume fraction and orientation strain.

2. Shear loading up to a maximum shear stress of 250 MPa (segment BC),
3. Compression up to a maximum compressive normal stress of 250 MPa (segment CD),
4. Shear reversal (segment DE),
5. Tensile loading up to a maximum tensile stress of 250 MPa (segment EF),
6. Unloading of shear stress (segment FG),
7. Unloading of tensile stress (segment GA), leading to complete unloading of the material.

The parameters used are those listed in table 5. The results of the simulation are reported in figure 8(b) as shear strain in terms of normal strain. An elastic response is also shown in the same figure for reference.

The evolution with the loading time of the martensite volume fraction and the orientation strain is shown in figure 9.

It is clear from the figures that the initial tensile loading is not sufficient

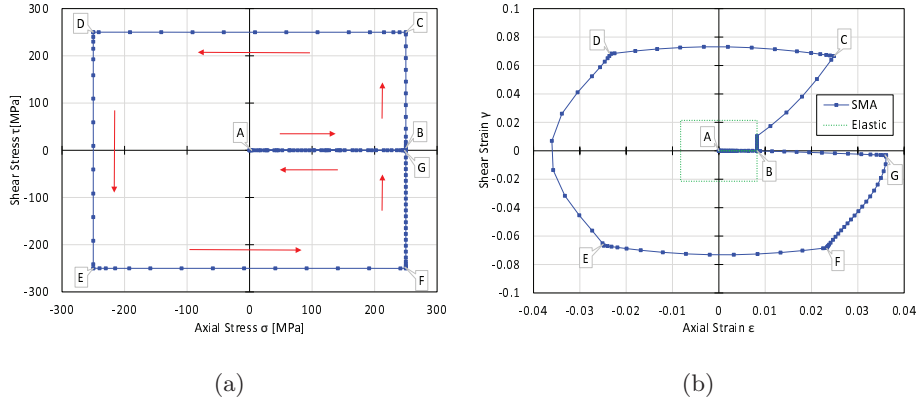


Figure 8: Biaxial non-proportional loading: (a) stress-controlled axial-shear loading, (b) shear versus axial strain response.

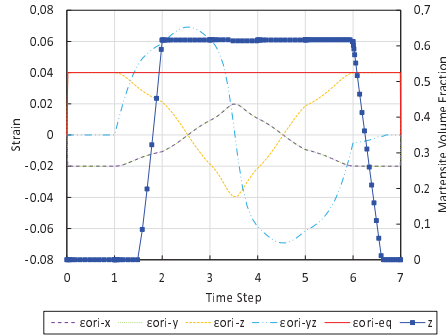


Figure 9: Evolution of the martensite volume fraction and orientation strain.

to cause inelastic deformation. The material behavior for loading step 1 therefore coincides with the reference elastic behavior. The superposition of shear in load step 2 increases the values taken by the loading functions for phase change and martensite reorientation leading to shear-dominated inelastic deformation as shown in figure 9. The onset of this deformation corresponds to a deviation from the vertical direction of the portion BC of the shear versus tensile strain curve in figure 8(b) as shear orientation strain starts to develop at the expense of normal strain (figure 9, step time 1–2).

Further tensile/shear loading in load steps 3 to 7 results in the evolution of the inelastic strain along the elliptic arcs CD, DE, EF and FG in figure 8(b). Complete strain recovery is then obtained upon complete unloading in load step 8. It can be observed that the strain at point G in figure 8(b), corresponding to time step 6 in figure 9, still comprises a residual shear component despite the removal of shear loading. This observation is a manifestation of martensite reorientation in presence of non-proportional loading, which results in the inelastic strain not being aligned with the stress. Despite the total inelastic strain being recoverable by unloading, individual strain components do not vanish if the corresponding stress components are unloaded. Rather, the components of the inelastic strain tensor are scaled down in magnitude when the volume fraction of martensite decreases. This is consistent with the physics of superelastic deformation in SMAs, where shape recovery results from the transformation of martensite into austenite, not from the inelastic deformation being recovered within the martensite phase.

4.3. Validation of the model

The model is used to simulate a number of cases reported in the literature involving superelastic shape memory alloys subjected to nonproportional loading. Both stress- and strain-controlled experiments are considered using data obtained by several research groups including Sittner et al. (1995), Bouvet et al. (2002), Stebner and Brinson (2013), Panico and Brinson (2007), Arghavani et al. (2010), Grabe and Bruhns (2009).

4.3.1. Strain-controlled tension-shear loading

Following the recently published work of Stebner and Brinson (2013), a SMA sample modelled as a single hexahedral mesh element, is subjected to

Parameter	Value	Parameter	Value
E_A	82675 MPa	a	4.79 MPa
E_M	35000 MPa	b	5.39 MPa
ν	0.4	ε_0	0.038
Y	30 MPa	G	4.48 MPa
α	789.5 MPa	β	3421 MPa
ξ	0.19 MPa	κ	2.32 MPa
A_f^0	300 K	T	340 K

Table 3: Parameters used for simulating SMA behavior in presence of nonproportional loading following Stebner and Brinson (2013).

the displacement-driven loading shown in figure 10(a). The loading involves nonproportional tensile-shear strain in which a maximum tensile strain of 0.04 is achieved. The material parameters used for the simulation, equivalent to those in Stebner and Brinson (2013), are listed in table 3. The temperature used for the simulation is artificial and is only meant to guarantee superelastic behavior of the shape memory alloy.

The displacement-controlled loading results in square-shaped shear strain versus normal strain behavior. The stress curve in figure 10(b) has a more complicated shape, which underlines the well-established nonlinearity in SMA behavior. Numerical simulations are in agreement with those obtained by Stebner and Brinson (2013). A better fit can likely be obtained by fine-tuning the parameters of the ZM model. Some deviation is inevitable however because of intrinsic differences between the two models.

The time evolution of the equivalent von Mises stress and the martensite volume fraction is shown in figure 11. Notable differences between the

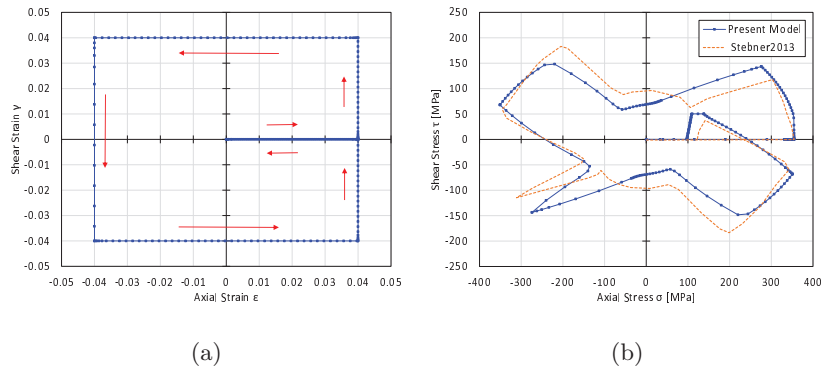


Figure 10: Numerical prediction of the stress and strain behavior of the SMA and comparison with numerical simulation results from (Stebner and Brinson, 2013).

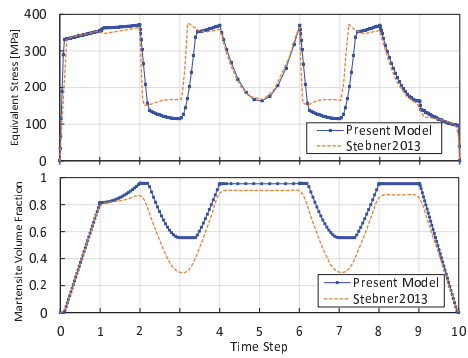


Figure 11: Evolution of the von Mises equivalent stress and martensite volume fraction with loading time.

simulation results of the two models include a steeper increase in the volume fraction of martensite from time step 1 to 2, which indicates that a more pronounced hardening is predicted by the ZM model leading to higher maximum value of the martensite volume fraction z at time step 2 that persists in subsequent load steps. In addition, the curve predicted by the ZM model features flat portions that indicate a delay in martensite reorientation with respect to changes in the loading direction. The delay is related to the formulation of the phase transformation function, which decreases slightly when the shear or tensile strain components decrease at the beginning of load steps 3, 4 and 8 (time steps 2-3, 3-4 and 7-8 respectively). The flat portions are indeed accompanied with a decrease of the von Mises equivalent stress, which strongly influences the phase transformation functions. Such decrease is not observed in the simulations of Stebner and Brinson (2013), which results in the absence of flat plateaus.

4.3.2. Strain-controlled tension-torsion loading

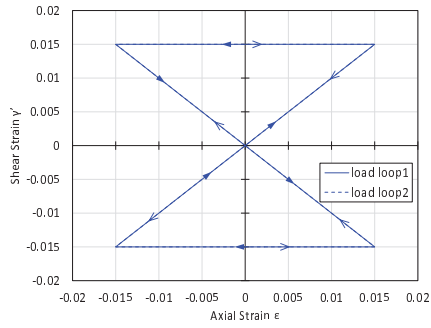
Experimental data reported by Grabe and Bruhns (2009) shows a strong dependence of the material behavior on the loading history. The loading considered by the authors is the one shown in figure 12(a), which consists in two strain-controlled butterfly loading paths that start and end at the same unloaded state. The maximum axial and shear strains reached in each case are $\varepsilon = \gamma' = \gamma/\sqrt{3} = 0.015$. Path 2 follows the loading sequence for path 1 in reverse order, such that the same intermediate states of shear and axial strain are achieved. The resulting material response in figure 12(b) shows a clear difference in terms of the shear versus axial stress curves corresponding to the two loading cases.

The experiments by Grabe and Bruhns (2009) are simulated using the

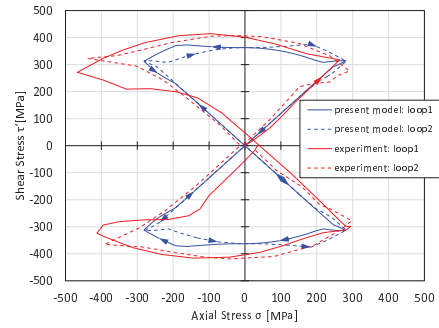
Parameter	Value	Parameter	Value
E_A	46800 MPa	a	0.85 MPa
E_M	18800 MPa	b	0.31 MPa
ν	0.3	ε_0	0.01
Y	30 MPa	G	2.19 MPa
α	2000MPa	β	5000 MPa
ξ	0.22 MPa	κ	0.6 MPa
A_f^0	300 K	T	340 K

Table 4: Parameters used for the simulations following Grabe and Bruhns (2009).

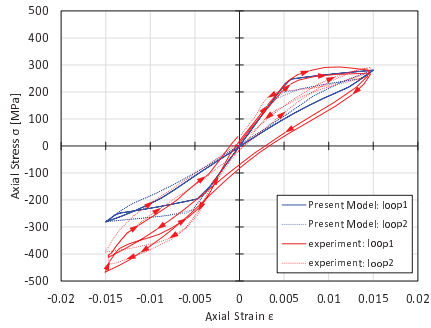
ZM model with the parameters listed in table 4. Since the original ZM model is used, in which asymmetry in the material behavior is not considered, the simulations could not predict the tensile-compressive asymmetry seen in figure 12(b). The overall agreement with the experimental data remains satisfactory nevertheless and does produce a trend similar to the one observed in the figure 12(b), where the first load path results in shear stresses with higher magnitudes in the second and third quadrants and lower magnitudes in the first and fourth quadrants compared to the shear stresses obtained with the second load path for extremal values $\gamma' = \pm 0.015$ of the shear strain. A good fit is also achieved for the stress-strain behavior in shear shown in figure 12(d). The difference between the experimental and simulation results is more pronounced, however, for the axial stress-strain curves in figure 12(c).



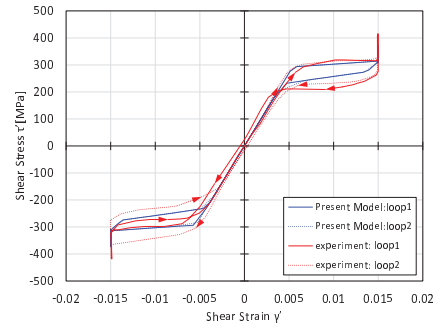
(a) Strain-controlled loading



(b) Shear vs. axial stress



(c) Stress-strain behavior in tension



(d) Stress-strain behavior in shear

Figure 12: Comparison of experimental and simulation results for the butterfly strain-controlled loading in figure 12(a).

4.3.3. Stress-controlled tension-torsion loading

Experimental data from Sittner et al. (1995) is used to validate the model for the case of nonproportional stress-controlled loading in tension and torsion. The experiments were carried out on thin-walled cylindrical SMA samples. The authors used the following expressions for the equivalent stress and strain in reporting their results:

$$\sigma_{eq} = \sqrt{\sigma^2 + \tau_{inv}^2} \qquad \tau_{inv} = C^S \tau, \qquad (44)$$

$$\varepsilon_{eq} = \sqrt{\varepsilon^2 + \gamma_{inv}^2} \qquad \gamma_{inv} = \frac{\gamma}{C^E}, \qquad (45)$$

where τ_{inv} and γ_{inv} are energetically equivalent shear stress and strain and C^S and C^E are empirical coefficients. von Mises equivalent stress and strain are obtained for $C^S = C^E = \sqrt{3}$. The above expressions for the equivalent stress and strain do not appear to be frame-invariant for the choice of C^S considered in the referenced paper. Since different expressions are used for σ_{eq} and ε_{eq} in the ZM model, two different loading cases are considered for the finite element simulations:

1. The first loading case is shown in figure 14(a), in which the normal and shear stress used for the simulation are exactly those reported in Sittner et al. (1995), but the equivalent stress is not the same.
2. The second loading case is shown in figure 16(a), in which the shear stress used for the simulation produces an equivalent stress identical to the one in Sittner et al. (1995).

For the first loading case, the material parameters used for the simulations are listed in table 5.

The parameters provide an acceptable fit of the uniaxial SMA response in tension and in shear as shown in figure 13. The experimental results of Sit-

Parameter	Value	Parameter	Value
E_A	30340 MPa	a	1.84 MPa
E_M	18000 MPa	b	1.3950 MPa
ν	0.3	ε_0	0.02
Y	30 MPa	G	11.46 MPa
α	1000 MPa	β	2500 MPa
ξ	0.116 MPa	κ	1.34 MPa
A_f^0	300 K	T	340 K

Table 5: Material parameters used for the simulation of nonproportional loading of SMAs following Sittner et al. (1995).

tner et al. (1995) as well as numerical simulations by Arghavani et al. (2010); Panico and Brinson (2007) are reported on the same figures for comparison. The results are in good agreement overall, with the model predictions being particularly consistent with those of Arghavani et al. (2010). This is likely because both the ZM model and the model by Arghavani et al. (2010) propose similar loading functions and evolution rules for the inelastic deformation of SMAs. Because of the intrinsically different expressions used for the equivalent stress and strain, it is not possible to accurately fit the material behavior in tension and shear simultaneously to those reported by Sittner et al.

In order to validate the model for the case of nonproportional loading, the loading shown in figure 14(a) is considered. The sample is first subjected to tensile loading corresponding to an increase in normal stress from 0 to 240 MPa. Shear is then applied up to a maximum shear stress of 195 MPa and then removed. The material behavior predicted by the model is shown in terms of shear versus axial strain in figure 14(b). The stress-strain behavior

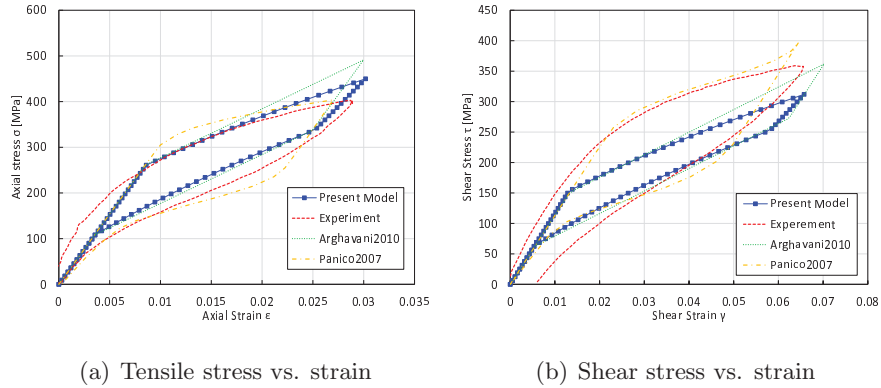
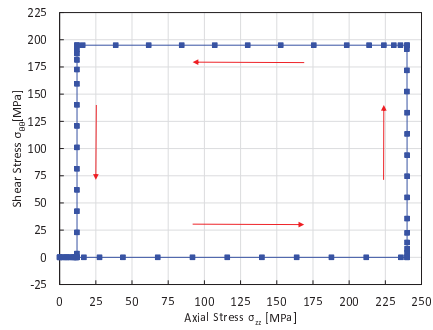
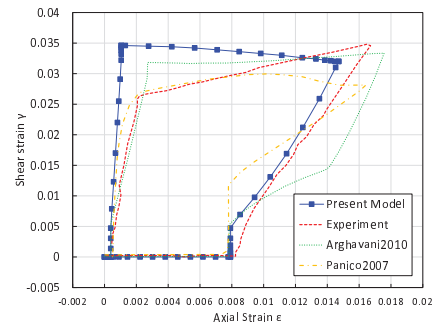


Figure 13: Tensile and shear stress-strain curves used to determine the parameters of the ZM model.

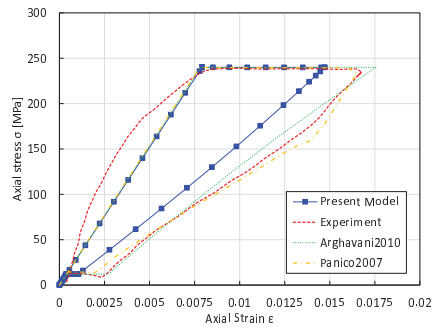
in tension and shear is shown in figures 14(c) and 14(d) respectively. In these figures, the results of numerical simulations using the ZM model are in good agreement overall with the experimental data and with the predictions of the other models considered. From figure 14(b), the material response appears to remain elastic throughout the tensile loading step and starts to become inelastic during the subsequent shear loading step where a deviation from the vertical direction is observed at an approximate shear strain of 0.005. In addition, it is interesting to observe that the predicted axial strain continues to increase during tensile unloading at constant shear stress, which is inconsistent with the experimental curve. A similar observation can also be made for the results obtained by Panico and Brinson (2007). The stress-strain behavior of the material in tension and in shear is shown in figures 14(c) and 14(d) respectively. In figure 14(c), it is interesting to see that the experimental curve appears to be nonlinear during the final unloading step, suggesting either an inelastic or a nonlinear elastic behavior of the material, which is not predicted by any of the models.



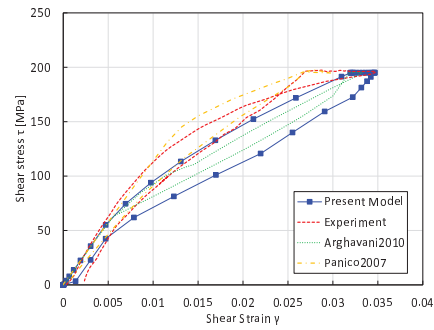
(a) Nonproportional loading



(b) Shear vs. axial strain



(c) Stress-strain behavior in tension



(d) Stress-strain behavior in shear

Figure 14: Experimental versus simulation results for the square tension-shear loading in figure 14(a).

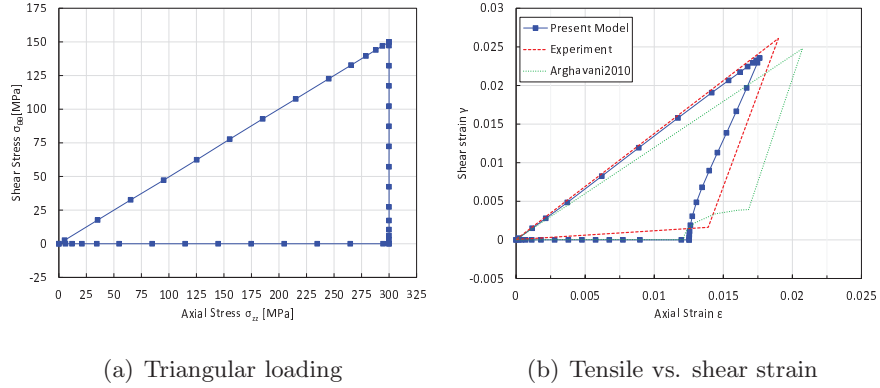


Figure 15: Experimental and simulation results for the triangular tension-shear loading in figure 15(a).

Further validation is shown in figure 15(b) considering the case of triangular loading in figure 15(a). The model predicts the experimental shear versus tensile strain curve to good accord. A notable deviation is observed during the tensile loading step, in which the material appears to develop shear strain in the absence of shear stress. Such behavior may be caused by an anisotropic behavior of the material, in which case a full stiffness tensor may result in the dependence of shear strain on normal stress. Another explanation could be an imprecise experimental setup or inaccurate data acquisition. For the second loading case shown in figure 16(a), the parameters of the model are those in table 6.

The parameters are chosen to properly fit the *equivalent* stress-strain curve in figure 16(e). As shown in figures 16(b) to 16(d), a better agreement with the experimental data is achieved in this case. Further validation is shown in figure 17(b) for the triangular loading in figure 17(a).

Parameter	Value	Parameter	Value
E_A	30000 MPa	a	0.99 MPa
E_M	18000 MPa	b	0.25 MPa
ν	0.3	ε_0	0.001
Y	30 MPa	G	3.5 MPa
α	2000 MPa	β	50000 MPa
ξ	0.0028 MPa	κ	0.97 MPa
A_f^0	300 K	T	340 K

Table 6: Material parameters used for simulating the experimental data in Sittner (1995) for the loading case in figure 16(a).

4.3.4. Stress-controlled tension-internal pressure loading

For this last validation, the reference experimental data are those obtained by Bouvet et al. (2002) for a tubular CuAlBe SMA sample subjected to nonproportional loading consisting of combined tension and internal pressure. The parameters used for the simulation are listed in table 3. They are determined using the tensile stress-strain curve in figure 18. The sample is subjected to the loading shown in figure 19(a), which corresponds to an increase in axial stress to 140 MPa, followed by an increase in the hoop stress to 140 MPa as well. The load is then removed in accordance with the square path shown.

The results are calculated by averaging along the thickness of the sample of the computed stress and strain for a point far from the two ends of the cylinder. The predicted strain response is shown in terms of hoop versus axial strain in figure 19(b). The simulated strain curve is in agreement with the experimental data and with numerical results from Arghavani et al. (2010). Strain curves corresponding to the interior and exterior surfaces of

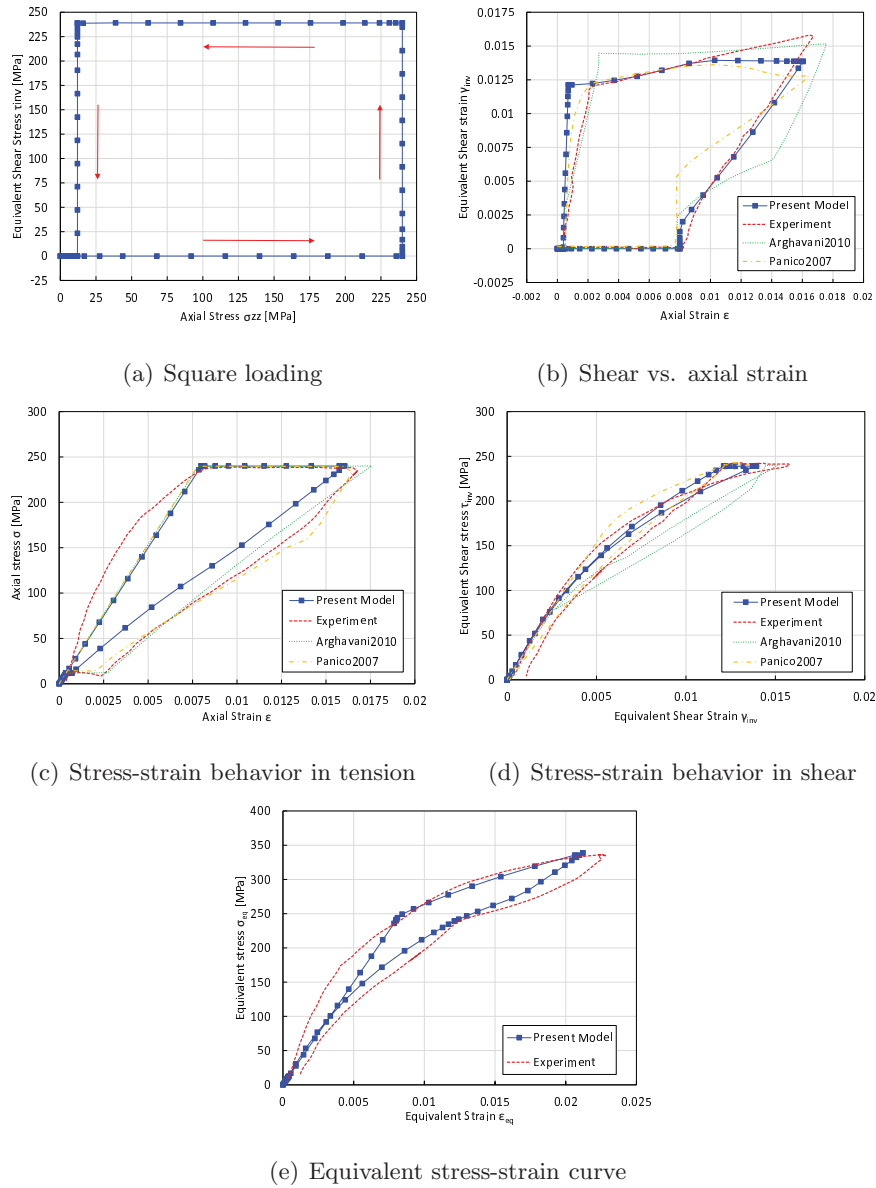
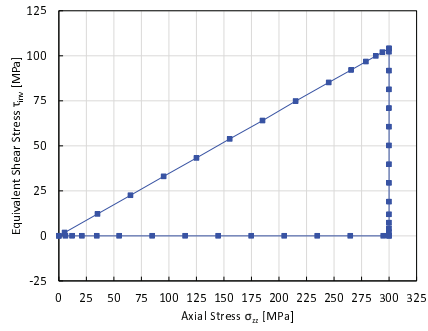
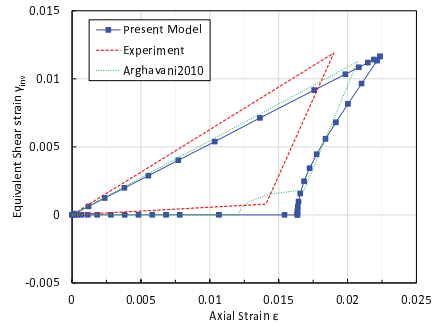


Figure 16: Experimental versus simulation results for the loading shown in figure 16(a).

the cylinder are shown for reference on the same figure. The simulation results that better represent the experimental data are those obtained for a



(a) Triangular loading



(b) Tensile vs. shear strain

Figure 17: Experimental versus simulation results for the triangular tension-shear loading in figure 17(a).

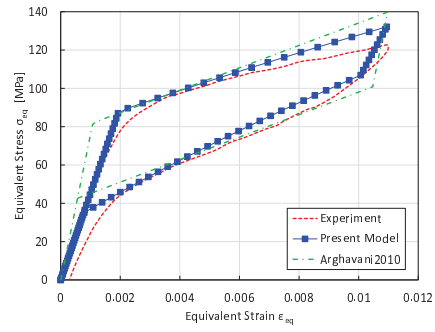


Figure 18: Uniaxial tensile curve used to determine the parameters of the ZM model.

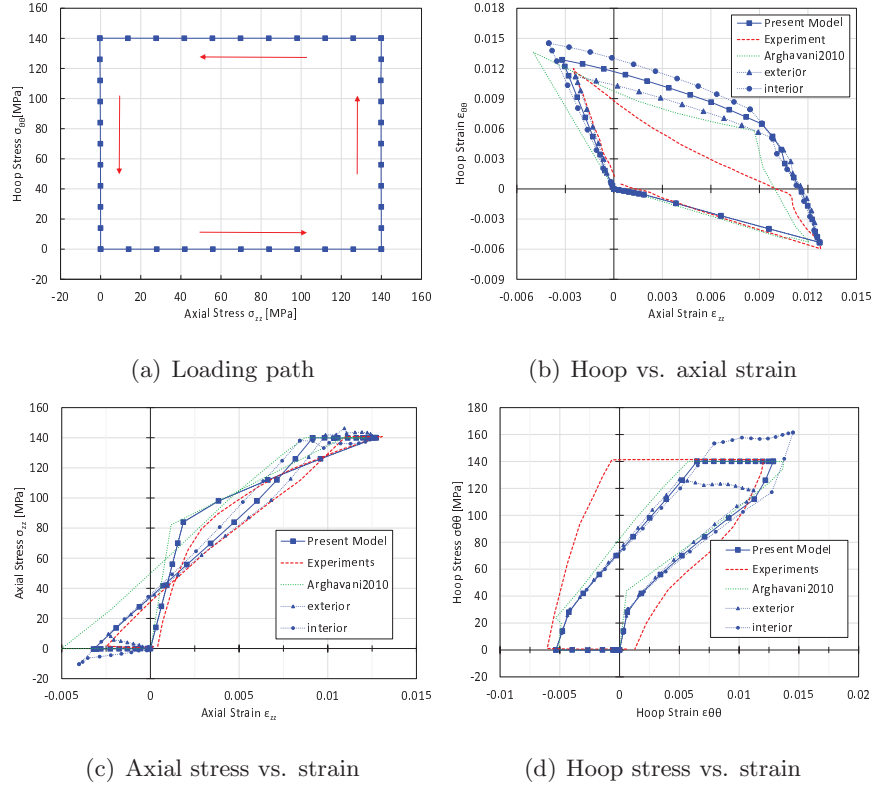


Figure 19: Simulation of the experimental data by Bouvet et al. (2002).

point located on the external wall of the sample. The curves present notable differences that result from the relatively low radius-to-thickness ratio of the sample used by Bouvet et al. (2002), which is 4.67. The assumption of a thin-walled cylinder may not therefore be adequate. The stress gradient across the thickness is indeed not negligible as shown in figure 20.

5. Conclusion

Numerical integration of the ZM model was presented in detail for the general case of SMAs undergoing phase transformation and martensite detwinning and reorientation. The proposed derivations include an analytical

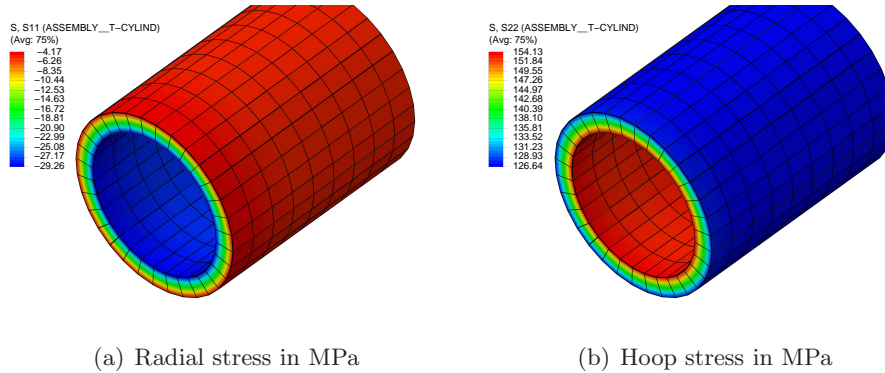


Figure 20: Stress variation in the radial direction for the cylinder used for numerical simulations.

expression for the continuous material Jacobian. The algorithmic aspects needed to properly detect active loading states for phase transformation and martensite reorientation, which may potentially take place at the same time, were properly explained. The algorithm was then implemented for use in finite element analysis by means of a user-material subroutine. The model was successfully used in predicting experimental and numerical data obtained by several research groups for SMA samples subjected to different types of multiaxial nonproportional loading. The samples ranged from a simple rectangular brick, meshed with a single linear element, to a Nitinol thin-wall cylinder. The loading cases considered varied from simple tension and shear, to combined loading involving tension, shear, and internal pressure leading to complex distributions of stress states within the material. In all these cases, the predictions of the model were in reasonable agreement with the reference data.

The proposed developments are part of an effort undertaken by the research team to develop numerical simulation capabilities that can be later used to analyze crack propagation and failure by fatigue of SMA devices in

presence of heterogeneous and multiaxial stress states.

Acknowledgements

Prof. Ziad Moumni would like to thank the 1000 Talent Plan and North-western Polytechnical University for their financial support. Dr. Wael Zaki would like to acknowledge the financial support of Khalifa University through KUIRF level 2 research fund no. 210031. Prof. Weihong Zhang would like to thank the National Natural Science Foundation of China (51221001), the National Basic Research Program of China (2012CB025904) and the 111 Project (B07050) for the financial support.

References

- J. Arghavani, F. Auricchio, R. Naghdabadi, A. Reali, and S. Sohrabpour. A 3-D phenomenological constitutive model for shape memory alloys under multiaxial loadings. *International Journal of Plasticity*, 26(7): 976–991, 2010. doi: <http://dx.doi.org/10.1016/j.ijplas.2009.12.003>. URL <http://www.sciencedirect.com/science/article/pii/S0749641909001648>.
- F. Auricchio, E. Bonetti, G. Scalet, and F. Ubertini. Theoretical and numerical modeling of shape memory alloys accounting for multiple phase transformations and martensite reorientation. *International Journal of Plasticity*, Mar 2014. ISSN 0749-6419. doi: 10.1016/j.ijplas.2014.03.008. URL <http://dx.doi.org/10.1016/j.ijplas.2014.03.008>.
- M. Bodaghi, A. R. Damanpack, M. M. Aghdam, and M. Shakeri. A phenomenological SMA model for combined axial-torsional proportional/non-proportional loading conditions. *Materials Science and Engineering: A*, 587(0):12–26, 2013.

doi: <http://dx.doi.org/10.1016/j.msea.2013.08.037>. URL
<http://www.sciencedirect.com/science/article/pii/S0921509313009246>.

- C. Bouvet, S. Calloch, and C. LExcellent. Mechanical Behavior of a Cu-Al-Be Shape Memory Alloy Under Multiaxial Proportional and Nonproportional Loadings. *Journal of Engineering Materials and Technology*, 124(2):112–124, 2002. doi: 10.1115/1.1448324. URL <http://dx.doi.org/10.1115/1.1448324>.
- C. Bouvet, S. Calloch, and C. LExcellent. A phenomenological model for pseudoelasticity of shape memory alloys under multiaxial proportional and nonproportional loadings. *European Journal of Mechanics - A/Solids*, 23(1):37–61, 2004. doi: <http://dx.doi.org/10.1016/j.euromechsol.2003.09.005>. URL <http://www.sciencedirect.com/science/article/pii/S0997753803001104>.
- Y. Chemisky, A. Duval, E. Patoor, and T. Ben Zineb. Constitutive model for shape memory alloys including phase transformation, martensitic reorientation and twins accommodation. *Mechanics of Materials*, 43(7): 361376, Jul 2011. ISSN 0167-6636. doi: 10.1016/j.mechmat.2011.04.003. URL <http://dx.doi.org/10.1016/j.mechmat.2011.04.003>.
- H. Funakubo. *Shape memory alloys*. Gordon and Breach Science Publishers, New York, 1987. ISBN 2881241360 9782881241369.
- C. Grabe and O. T. Bruhns. Path dependence and multiaxial behavior of a polycrystalline NiTi alloy within the pseudoelastic and pseudo-plastic temperature regimes. *International Journal of Plasticity*, 25(3): 513–545, 2009. doi: <http://dx.doi.org/10.1016/j.ijplas.2008.03.002>. URL <http://www.sciencedirect.com/science/article/pii/S0749641908000387>.

- B. Halphen and Q. S. Nguyen. Plastic and visco-plastic materials with generalized potential. *Mechanics Research Communications*, 1(1): 43–47, 1974. doi: [http://dx.doi.org/10.1016/0093-6413\(74\)90034-2](http://dx.doi.org/10.1016/0093-6413(74)90034-2). URL <http://www.sciencedirect.com/science/article/pii/0093641374900342>.
- J. V. Humbeeck. Non-medical applications of shape memory alloys. *Materials Science and Engineering: A*, 273275(0):134 – 148, 1999. ISSN 0921-5093. doi: [http://dx.doi.org/10.1016/S0921-5093\(99\)00293-2](http://dx.doi.org/10.1016/S0921-5093(99)00293-2). URL <http://www.sciencedirect.com/science/article/pii/S0921509399002932>.
- T. J. Lim and D. L. McDowell. Mechanical Behavior of an Ni-Ti Shape Memory Alloy Under Axial-Torsional Proportional and Nonproportional Loading. *Journal of Engineering Materials and Technology*, 121(1):9–18, 1999. doi: 10.1115/1.2816007. URL <http://dx.doi.org/10.1115/1.2816007>.
- R. Mehrabi, M. Kadkhodaei, and M. Elahinia. A thermodynamically-consistent microplane model for shape memory alloys. *International Journal of Solids and Structures*, Apr 2014. ISSN 0020-7683. doi: 10.1016/j.ijsolstr.2014.03.039. URL <http://dx.doi.org/10.1016/j.ijsolstr.2014.03.039>.
- C. Morin. *A comprehensive approach for fatigue analysis of shape memory alloys*. PhD thesis, École Polytechnique, 2011.
- C. Morin, Z. Moumni, and W. Zaki. A constitutive model for shape memory alloys accounting for thermomechanical coupling. *International Journal of Plasticity*, 27(5):748–767, 2011a. doi: <http://dx.doi.org/10.1016/j.ijplas.2010.09.005>. URL <http://www.sciencedirect.com/science/article/pii/S0749641910001312>.

- C. Morin, Z. Moumni, and W. Zaki. Thermomechanical coupling in shape memory alloys under cyclic loadings: Experimental analysis and constitutive modeling. *International Journal of Plasticity*, 27(12):1959–1980, 2011b. doi: <http://dx.doi.org/10.1016/j.ijplas.2011.05.005>. URL <http://www.sciencedirect.com/science/article/pii/S0749641911000817>.
- C. Morin, Z. Moumni, and W. Zaki. Direct numerical determination of the asymptotic cyclic behavior of pseudoelastic shape memory structures. *Journal of Engineering Mechanics*, 137(7):497 – 503, 2011c.
- Z. Moumni. *Sur la modélisation du changement de phase à l'état solide*. PhD thesis, ENPC, 1995.
- Z. Moumni, W. Zaki, and Q. S. Nguyen. Theoretical and numerical modeling of solid-solid phase change: Application to the description of the thermomechanical behavior of shape memory alloys. *International Journal of Plasticity*, 24(4):614–645, 2008. doi: <http://dx.doi.org/10.1016/j.ijplas.2007.07.007>. URL <http://www.sciencedirect.com/science/article/pii/S0749641907000988>.
- Z. Moumni, W. Zaki, and H. Maïtournam. Cyclic behavior and energy approach to the fatigue of shape memory alloys. *Journal of Mechanics of Materials and Structures*, 4:395–411, 2009.
- K. Otsuka and C. Wayman. *Shape Memory Materials*. Cambridge University Press, 1999. ISBN 9780521663847.
- M. Panico and L. C. Brinson. A three-dimensional phenomenological model for martensite reorientation in shape memory alloys. *Journal of the Mechanics and Physics of Solids*, 55(11):2491–2511,

2007. doi: <http://dx.doi.org/10.1016/j.jmps.2007.03.010>. URL <http://www.sciencedirect.com/science/article/pii/S0022509607000713>.

- E. Patoor, D. Lagoudas, P. Entchev, C. Brinson, and G. Xiujie. Shape memory alloys, part I: general properties. *Mechanics of Materials*, 38 (5-6):391-429, 2006.
- J. Simo and T. Hughes. *Computational Inelasticity*, volume 7. Springer, 1998.
- P. Sittner, Y. Hara, and M. Tokuda. Experimental study on the thermoelastic martensitic transformation in shape memory alloy polycrystal induced by combined external forces. *Metallurgical and Materials Transactions A*, 26(11):2923-2935, 1995. doi: 10.1007/BF02669649. URL <http://dx.doi.org/10.1007/BF02669649>.
- A. P. Stebner and L. C. Brinson. Explicit finite element implementation of an improved three dimensional constitutive model for shape memory alloys. *Computer Methods in Applied Mechanics and Engineering*, 257 (0):17-35, 2013. doi: <http://dx.doi.org/10.1016/j.cma.2012.12.021>. URL <http://www.sciencedirect.com/science/article/pii/S0045782513000042>.
- D. Stöckel. Nitinol medical devices and implants. Technical report, Cordis Corporation - Nitinol Devices & Components, 2001.
- W. Zaki. An approach to modeling tensile-compressive asymmetry for martensitic shape memory alloys. *Smart Materials and Structures*, 2010.
- W. Zaki. Time integration of a model for martensite detwinning and reorientation under nonproportional loading using Lagrange multipliers. *International Journal of Solids and Structures*, 49(21):2951-2961,

2012a. doi: <http://dx.doi.org/10.1016/j.ijsolstr.2012.05.038>. URL <http://www.sciencedirect.com/science/article/pii/S002076831200265X>.

W. Zaki. An efficient implementation for a model of martensite reorientation in martensitic shape memory alloys under multi-axial nonproportional loading. *International Journal of Plasticity*, 37:72–94, 2012b. doi: 10.1016/j.ijplas.2012.04.002. URL <Go to ISI>://WOS:000307416100005.

W. Zaki and Z. Moumni. A three-dimensional model of the thermomechanical behavior of shape memory alloys. *Journal of the Mechanics and Physics of Solids*, 55(11):2455–2490, Nov. 2007a.

W. Zaki and Z. Moumni. A 3D model of the cyclic thermomechanical behavior of shape memory alloys. *Journal of the Mechanics and Physics of Solids*, 55(11):2427–2454, Nov. 2007b.

W. Zaki, S. Zamfir, and Z. Moumni. An extension of the ZM model for shape memory alloys accounting for plastic deformation. *Mechanics of Materials*, 42(3):266 – 274, 2010. ISSN 0167-6636. doi: DOI:10.1016/j.mechmat.2009.11.013.

W. Zaki, Z. Moumni, and C. Morin. Modeling tensile-compressive asymmetry for superelastic shape memory alloys. *Mechanics of Advanced Materials and Structures*, 18(7):559–564, 2011.